Frontiers of Information Technology & Electronic Engineering
www.jzus.zju.edu.cn; engineering.cae.cn; www.springerlink.com
ISSN 2095-9184 (print); ISSN 2095-9230 (online)
E-mail: jzus@zju.edu.cn

Multi-feed multi-mode metasurface for independent orbital angular momentum communication in dual polarization*

Lingjun YANG[1], Sheng SUN[†‡1], Wei E.I. SHA[2], Long LI[3], Jun HU[1]

[1]*School of Electronic Science and Engineering, University of Electronic Science and Technology of China, Chengdu 611731, China*

[2]*College of Information Science & Electronic Engineering, Zhejiang University, Hangzhou 310027, China*

[3]*School of Electronic Engineering, Xidian University, Xi'an 710071, China*

[†]E-mail: sunsheng@ieee.org

Received Oct. 15, 2022; Revision accepted Feb. 2, 2023; Crosschecked Oct. 26, 2023

Abstract: The wavefront control of spin or orbital angular momentum (OAM) is widely applied in the optical and radio fields. However, most passive metasurfaces provide limited manipulations, such as the spin-locked wavefront, a static OAM combination, or an uncontrollable OAM energy distribution. We propose a reflection-type multi-feed metasurface to independently generate multi-mode OAM beams with dynamically switchable OAM combinations and spin states, while simultaneously, the energy distribution of carrying OAM modes is controllable. Specifically, four elements are proposed to overcome the spin-locked phase limitation by combining propagation and geometric phases. The robustness of these elements is analyzed. By involving the amplitude term and multi-feed technology in the design process, the proposed metasurface can generate OAM beams with a controllable energy distribution over modes and switchable mode combinations. OAM-based radio communication with four independent channels is experimentally demonstrated at 14 GHz by employing a pair of the proposed metasurfaces. The powers of different channels are adjustable by the provided amplitude term, and the maximum crosstalk is −9 dB, proving the effectiveness and practicability of the proposed method.

Key words: Orbital angular momentum (OAM); Geometric phase; Multi-feed metasurface; Spin-decoupled metasurface; Vortex beam communication

https://doi.org/10.1631/FITEE.2200471 **CLC number:** O441

1 Introduction

Orbital angular momentum (OAM) has received great interest since it was applied in the optics field (Allen et al., 1992). Vortex beams carrying OAM are characterized by a doughnut-shaped pattern and a helical phase wavefront with the azimuthal phase term of $e^{jl\varphi}$, where l is the OAM mode and φ is the azimuthal angle around the propagation axis. Compared with the spin angular momentum associated with the left and right circularly polarized (CP) waves that offer only limited channels, OAM can provide more orthogonal modes (Mohammadi et al., 2010). Therefore, OAM beams have been applied in optical (Wang J et al., 2012), fiber (Bozinovic et al., 2013), radio (Tamagnone et al., 2012; Yan et al., 2014; Zhang WT et al., 2017), and acoustic (Jiang X et al., 2018) communications to further expand communication capacity. Although there are still controversies concerning OAM far-field communication and OAM communication advantages over the multiple-input-multiple-output technology (Edfors and Johansson, 2012; Yuan SSA

‡ Corresponding author

* Project supported by the National Natural Science Foundation of China (Nos. 61971115, 61721001, 61975177, and 61971099)

ORCID: Lingjun YANG, https://orcid.org/0000-0002-5964-4308; Sheng SUN, https://orcid.org/0000-0003-2684-9662; Wei E.I. SHA, https://orcid.org/0000-0002-7431-8121; Long LI, https://orcid.org/0000-0003-0472-7314; Jun HU, https://orcid.org/0000-0002-4565-3000

et al., 2021), many useful applications have been reported in the literature including super-resolution imaging (Liu K et al., 2017), structure field formation (Barbuto et al., 2017, 2021), optical tweezers (Han and Grier, 2003), and astronomy (Uribe-Patarroyo et al., 2011). Thidé et al. (2007) proposed uniform circular antenna arrays to generate vortex beams in the microwave frequency range. Since then, many microwave OAM generators have been proposed, such as traveling-wave antennas (Zhang ZF et al., 2017), spiral phase plates (Chen YL et al., 2016), and antenna arrays (Liu K et al., 2016; Lin et al., 2017; Kang et al., 2019). However, there is an urgent need to minimize the size, mass, and power requirements of the generators. Recently, some artificial interfaces named metasurfaces have been proposed to address those problems.

Metasurfaces, composed of artificial elements with subwavelength thicknesses, show great potential in manipulating the polarization, phase, and amplitude of electromagnetic fields (Yu NF et al., 2011; Sun et al., 2012; Zhang XG et al., 2020; Pitilakis et al., 2022; Vellucci et al., 2022; Yang et al., 2022). Many OAM metasurfaces (Yu SX et al., 2016a, 2016b; Chen MLN et al., 2017, 2019; Zhang K et al., 2018; Akram Z et al., 2019; Ma et al., 2019; Tian et al., 2019; Bai et al., 2020; Sroor et al., 2020) have been proposed to convert plane waves into expected vortex beams. Those metasurface-based ultra-thin devices offer significant advantages over conventional OAM generators. In particular, based on the geometric phase theory, some ultra-thin metasurfaces have been proposed to generate broadband OAM beams for a specific CP wave (Luo et al., 2017; Xu et al., 2017; Tang et al., 2019; Akram MR et al., 2020; Yang et al., 2023). Nevertheless, the obtained phase profiles for two orthogonal CP waves are inversed due to the intrinsically opposite signs for the two spins, constraining the other CP wave to be in the opposite OAM mode. This spin-locked control would significantly hinder actual dual-CP applications. Recently, spin-decoupled metasurfaces were proposed to independently control different CP waves, where the phase profiles for orthogonal CP waves can be independently designed by combining the geometric phase with the propagation phase (Devlin et al., 2017; Mueller et al., 2017; Xu et al., 2020; Wang ZX et al., 2021; Ding et al., 2022). In the microwave region, those ultra-thin spin-decoupled metasurfaces can be easily fabricated using conventional printed circuit board (PCB) techniques. For instance, Ding et al. (2022) proposed a two-dielectric-layer metasurface with a thickness of 3.26 mm to generate spin-decoupled OAM vortices independently. Some single-layer spin-decoupled metasurfaces have also been reported with thicknesses of 3.5 mm (Guo et al., 2020b) and 2.5 mm (Guo et al., 2020a). Despite these successful implementations, the detailed design of the element texture and thickness is worthy of further investigation, and efforts should be devoted to designing a robust element.

On the other hand, independent control of multiple OAM modes is essential for multi-mode multiplexing in modern wireless communications. Unfortunately, the multi-mode vortex beams generated by single-feed passive metasurfaces have a static mode combination (Liu HQ et al., 2018; Bao et al., 2020; Jiang ZH et al., 2020; Yuan YY et al., 2020), limiting their practical applications. A programing metasurface loaded with active components can generate OAM beams with electronically controlled modes (Li LL et al., 2017; Shuang et al., 2020). However, such loading makes the element more complicated, especially for multi-bit coding elements. More recently, some multi-feed metasurfaces have been proposed to independently control OAM modes (Li SQ et al., 2020; Zhang S et al., 2020; Feng et al., 2022), but they work in either single polarization or the optical band. Moreover, their energy distribution between OAM modes is uncontrollable.

In this paper, we propose a multi-feed spin-decoupled metasurface to independently tune two CP wavefronts with dynamic OAM combinations and controllable OAM energy distribution. In particular, four ultra-thin geometric-phase elements are proposed to engineer a spin-decoupled metasurface that can independently generate energy-controllable OAM beams in two orthogonal circular polarizations (Fig. 1a). Furthermore, by involving the multi-feed design in the metasurface, the OAM modes and CP states of generated beams are dynamically switchable. This metasurface ultimately achieves independent control over both spin and orbital angular momenta. Eventually, an OAM-based four-channel system is experimentally demonstrated with controllable channel powers and low crosstalk in dual-CP states, verifying our independent control of spin states and OAM states.

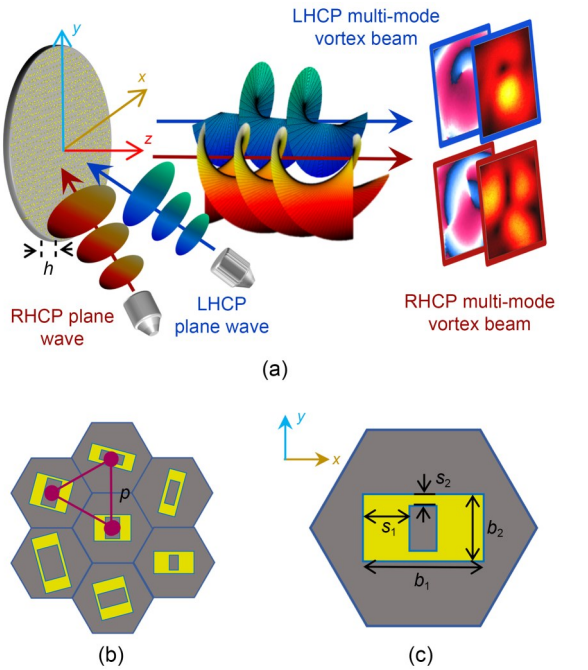

Fig. 1 Schematic of vortex wave generation device: (a) schematic of a multi-mode metasurface with independent spin-to-orbital angular momentum conversion; (b) topological structure of the arrangement; (c) specific element structure (LHCP: left-handed circularly polarized; RHCP: right-handed circularly polarized)

2 Theory and methods

This section aims to present the theory and methods for engineering a multi-feed spin-decoupled multi-mode metasurface.

2.1 Theory of independent control over circularly polarized wavefronts

The theory of independent control over CP waves (also called the spin-decoupled strategy) has been proposed by combining the geometric phase and propagation phase. The geometric phase also known as the Pancharatnam–Berry phase (Berry, 1984) is an additional phase factor of scattered waves triggered by rotating the orientation angle ϕ of the scattering element. It is convenient to illustrate the link between the geometric phase and the orientation angle ϕ using the Jones calculus. Based on the Jones calculus, the reflected and incident fields can be connected by the reflection coefficients in the reflected Jones matrix. If the element is mirror-symmetric with respect to the *yz*- or *xz*-plane, the cross-polarized reflection coefficients r_{xy} and r_{yx} satisfy $r_{xy}=r_{yx}=0$ (Menzel et al., 2010). By adjusting the amplitude of co-polarized reflection coefficients to unity ($|r_{xx}|=|r_{yy}|=1$) but with a π phase difference ($\varphi_{xx}-\varphi_{yy}=\pi$), the CP reflection coefficients can be simplified as

$$r_{\mathrm{ll}} = 0.5(r_{xx} - r_{yy})\mathrm{e}^{-\mathrm{j}2\phi} = \mathrm{e}^{\mathrm{j}(\varphi_{xx} - 2\phi)}, \quad (1a)$$

$$r_{\mathrm{lr}} = 0.5(r_{xx} + r_{yy}) = 0, \quad (1b)$$

$$r_{\mathrm{rl}} = 0.5(r_{xx} + r_{yy}) = 0, \quad (1c)$$

$$r_{\mathrm{rr}} = 0.5(r_{xx} - r_{yy})\mathrm{e}^{\mathrm{j}2\phi} = \mathrm{e}^{\mathrm{j}(\varphi_{xx} + 2\phi)}, \quad (1d)$$

where subscripts l and r refer to left-handed circularly polarized (LHCP) and right-handed circularly polarized (RHCP), respectively. Eqs. (1a) and (1d) show the ideal phase responses for a geometric-phase element, where the CP phases of co-polarized reflection coefficients (φ_{ll} and φ_{rr}) can be determined by the orientation angles ϕ and φ_{xx}. We can write down the odd and even phases for the CP phases as follows:

$$\varphi_{\mathrm{odd}} = (\varphi_{\mathrm{rr}} - \varphi_{\mathrm{ll}})/2 = 2\phi, \quad (2a)$$

$$\varphi_{\mathrm{even}} = (\varphi_{\mathrm{rr}} + \varphi_{\mathrm{ll}})/2 = \varphi_{xx}. \quad (2b)$$

The two CP phases are decomposed into odd and even phases. Arbitrary CP phases can be obtained if one can freely design both the even and odd phases across a 2π range. As seen from Eq. (2a), the geometric phase provides arbitrary odd phase control, in which phase difference can be freely controlled over a 2π range by the angular orientation ϕ. Thus, an independent CP wave can be obtained if one can freely design the even phase (φ_{even} or φ_{xx}) over a 2π range.

2.2 Specific design of elements

This subsection aims to fabricate a set of robust elements with a 2π range of even (propagation) phase simultaneously possessing a high-efficiency geometric phase character. The robust performance is reflected in a high conversion efficiency and minor phase sensitivity. The specific design procedure is demonstrated step-by-step as follows.

2.2.1 Arrangement and structure of elements

A single-dielectric-layer substrate is applied to maintain simple and ultra-thin features. The broadband single-dielectric-layer element with rectangular-ring texture (Yang et al., 2020) is a good candidate for our design, in which the 180° phase difference and the

flat phase response are satisfied in a broad bandwidth. On the other hand, the triangular arrangement of hexagonal elements is widely used in antenna arrays (Pogorzelski, 2004) and metasurfaces (Sievenpiper et al., 1999) by virtue of its compact structure and isotropy. Compared with the square lattice in geometric-phase metasurfaces, the triangular arrangement of hexagonal elements has been shown to weaken the coupling fluctuation (Yang et al., 2021). Consequently, the triangular arrangement of the rectangular-ring structure is a good prototype for designing our spin-decoupled elements; the specific topological structure is shown in Fig. 1b.

2.2.2 Analysis of the thickness and substrate

Fig. 1c shows the specific rectangular-ring element. The rectangular-ring structure on the top is copper with a thickness of 0.018 mm, which is supported by a substrate layer with a thickness of h. The bottom of the substrate layer is metal ground to achieve a total reflection. The initial parameters are p=10 mm, b_1=7.6 mm, s_1=1.5 mm, b_2=3.6 mm, and s_2=0.3 mm. A proper selection of thickness (h) and substrate (ε_r) is crucial to meet the flat phase response for our robust elements. Simulation results are calculated in commercial software High Frequency Structure Simulator (HFSS), and the specific setup can be found in Yang et al. (2021). Fig. 2 shows the simulation results of the reflection coefficient as a function of ε_r and h (only r_{yy} is demonstrated due to similarity). As seen in Fig. 2a, the real part of the dielectric Re(ε_r) mainly affects the resonance frequency. However, a substrate with Im(ε_r)=0.02 can trigger a more than 4 dB amplitude attenuation at the resonant frequency. Thus, a low-loss substrate is necessary. On the other hand, the thickness (h) of the substrate significantly affects the resonance, as seen in Fig. 2b. The phase responses at the resonant frequency become steeper as the thickness decreases. The flat phase response is highly expected to shape the robust elements, whereas the phase error triggered by fabrication is tiny. To balance the robust and ultrathin feature, we select the substrate as F4B (ε_r=2.65+0.002i) with a thickness of h=2 mm in this study.

2.2.3 Spin-decoupled elements and the corresponding phase stability

The rectangular-ring elements in mentioned paper (Yang et al., 2021) are geometric phase only. Here, we involve the dimension-related change of the rectangular-ring structure to achieve additional propagation-phase control. By scanning the parameters of b_1 and b_2, the linearly polarized phase responses at 14 GHz are shown in Fig. 3. "∠" is to measure the argument of a complex

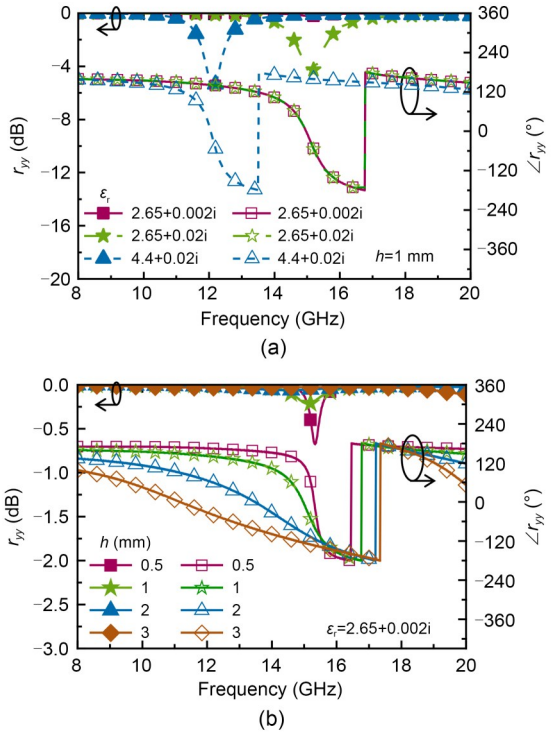

Fig. 2 Simulated reflection amplitudes and phase responses of element for *y*-polarization: (a) with different dielectric constants and losses; (b) with different thicknesses

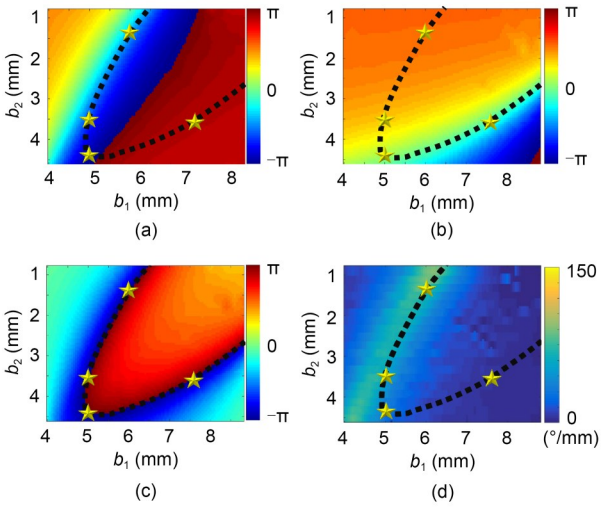

Fig. 3 Simulated reflection phase responses of the element with different geometric parameters of b_1 and b_2: (a) $\angle r_{xx}$; (b) $\angle r_{yy}$; (c) $\angle r_{xx}-\angle r_{yy}$; (d) $\mathrm{d}(\angle r_{xx})/\mathrm{d}b_2$

number. The dashed lines in Fig. 3 depict the geometric phase elements, where a π phase difference is satisfied precisely between the *x*- and the *y*-polarization as seen in Fig. 3c. Simultaneously, four specific elements (marked by four stars) can be selected to quantize a π phase range of even phase, as seen in Fig. 3a. Although four elements are selected in this case, more additional elements on the dashed lines could be involved to reduce the quantization error. Here, the phase stability of these elements is investigated. As depicted in Fig. 3d, the partial derivative of the phase response to the geometric parameter is below 15°/0.1 mm (take $\mathrm{d}(\angle r_{xx})/\mathrm{d}b_2$ as an example in this study). It is crucial for practical applications because the low phase sensitivity will minimize phase errors caused by fabrication tolerances.

Two tips can be useful for selecting these high-robustness elements: designing elements with flat phase response and avoiding selecting elements with sharp phase gradients.

The parameters of the four selected elements are b_1=5.0, 5.0, 6.0, and 7.6 mm, b_2=4.4, 3.6, 1.4, and 3.6 mm. By rotating the element with ϕ=90°, a π phase difference can be imparted to the original even phase. Therefore, we can apply the eight elements to cover the even phase from −π to π. The corresponding phase responses and polarization conversion ratio (PCR) of the eight elements are shown in Fig. 4. PCR is used to reflect the conversion efficiency of elements. This parameter can be calculated in the following equation:

$$\mathrm{PCR}=\frac{|r_{\mathrm{ll}}|^2}{|r_{\mathrm{ll}}|^2+|r_{\mathrm{rl}}|^2}. \tag{3}$$

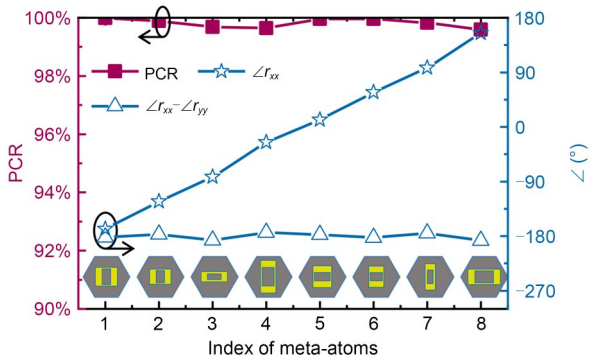

Fig. 4 Corresponding phase responses and polarization conversion ratio (PCR) of the selected eight elements

Note that all the PCR is higher than 99.5% (nearly 100% efficiency) in Fig. 4, which is particularly important for dual-CP applications.

2.3 Theoretical verification of multi-mode vortex beams

According to the Huygens–Fresnel theory, the radiation field generated by the metasurface could be estimated by the superposition of the secondary wavelets emanating from different elements. We can theoretically calculate the radiation field as follows:

$$\begin{cases}\boldsymbol{E}_{\mathrm{rad}}(\boldsymbol{r})=E_{\mathrm{rad}}(\boldsymbol{r})\boldsymbol{e}_{\mathrm{cp}}=\sum_{i}^{N_{\mathrm{t}}}\dfrac{B}{4\pi R}\mathrm{e}^{-\mathrm{j}kR+\mathrm{j}\Phi(\boldsymbol{r}_i')}\boldsymbol{e}_{\mathrm{cp}},\\ R=\left|\boldsymbol{r}-\boldsymbol{r}_i'\right|,\end{cases} \tag{4}$$

where $\boldsymbol{r}_i'$ is the position vector of the i^{th} element, $\boldsymbol{r}$ is the position vector of the field point, and $\boldsymbol{e}_{\mathrm{cp}}$ is the unit vector of the interested CP. N_{t} is the total number of elements, which can be calculated once the aperture (with diameter D) of the metasurface is determined. According to the Huygens–Fresnel theory, the inclination factor B given by Kirchhoff satisfies B=jk(1+cosθ). $\Phi(\boldsymbol{r}_i')$ is the phase profile of metasurfaces, which is the key point for generating vortex beams. In this study, the magnitude variation is neglected for our phase-only metasurface, which may trigger some crosstalk modes in generating the superimposed OAM beams (Zhu and Wang, 2015; Yang et al., 2022). This choice is good enough to generate the desired OAM beams. By imparting a multi-mode phase profile $\Phi(\boldsymbol{r}_i')=\Phi^l(\varphi_i')$ on metasurfaces, a multi-mode vortex beam can be generated:

$$\Phi^l(\varphi_i')=\angle\left(\sum_m a_m\mathrm{e}^{\mathrm{j}l_m\varphi_i'}\right), \tag{5}$$

where m is the number of channels, and l_m is the corresponding OAM mode. a_m is the corresponding amplitude term, which can be used to control the energy weight of different modes. θ and φ are the polar angle and azimuth angle under spherical coordinate, respectively. Substituting Eq. (5) in Eq. (4), a theoretical result of the radiation field can be predicted by means of which one can precisely design the parameters of the metasurface rather than using a time-consuming simulation. Fig. 5 shows three normalized radiation

fields in the *xz*-plane generated by Eq. (4) for l=1 metasurfaces with different apertures. It can be seen in Fig. 5 that the generated OAM beams have a cone-shaped pattern with zero intensity in the center. An enlarged aperture (D) of our transmitting metasurface will reduce the divergence and increase the field density of the generated vortex beams. Importantly, the cone angles and the beam paths in different cases can be displayed vividly, which is significant for selecting an appropriate position and a sufficiently sizeable receiving plane to receive the main lobe of the generated conical OAM beam. For example, a receiving aperture of 300 mm is large enough to receive the l=1 vortex beam generated by a transmitting aperture of 300 mm at a distance of 2000 mm.

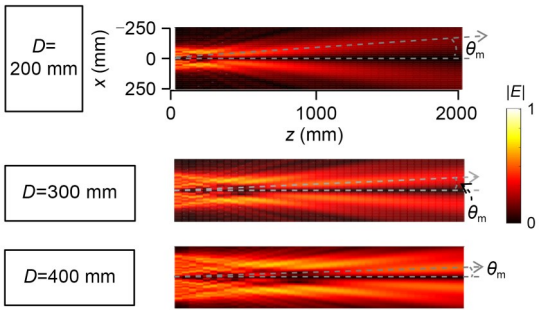

Fig. 5 Numerical results of the l=1 vortex beam in the *xz*-plane generated by Eq. (4) with different apertures of transmitting metasurfaces. θ_m is the cone angle (main lobe) of the generated vortex beams

In this study, the apertures of transmitting and receiving metasurfaces are with D=300 mm. The observation or receiving plane is selected at z=2000 mm, which is located at a radiative near-field region. The distance can be further increased by enlarging the size of the transmitting or receiving metasurface. Fig. 6 further demonstrates some theoretical results at the observation plane calculated by Eq. (4) under different cases for l_m and a_m. Case I shows the generated single-mode vortex beam, and the amplitude profile presents as a doughnut-shaped pattern. The pictures in cases I, II, and III depict the generated vortex beams from single-mode to multi-mode case (doughnut-shape to chipped-doughnut-shape pattern). As the amplitude

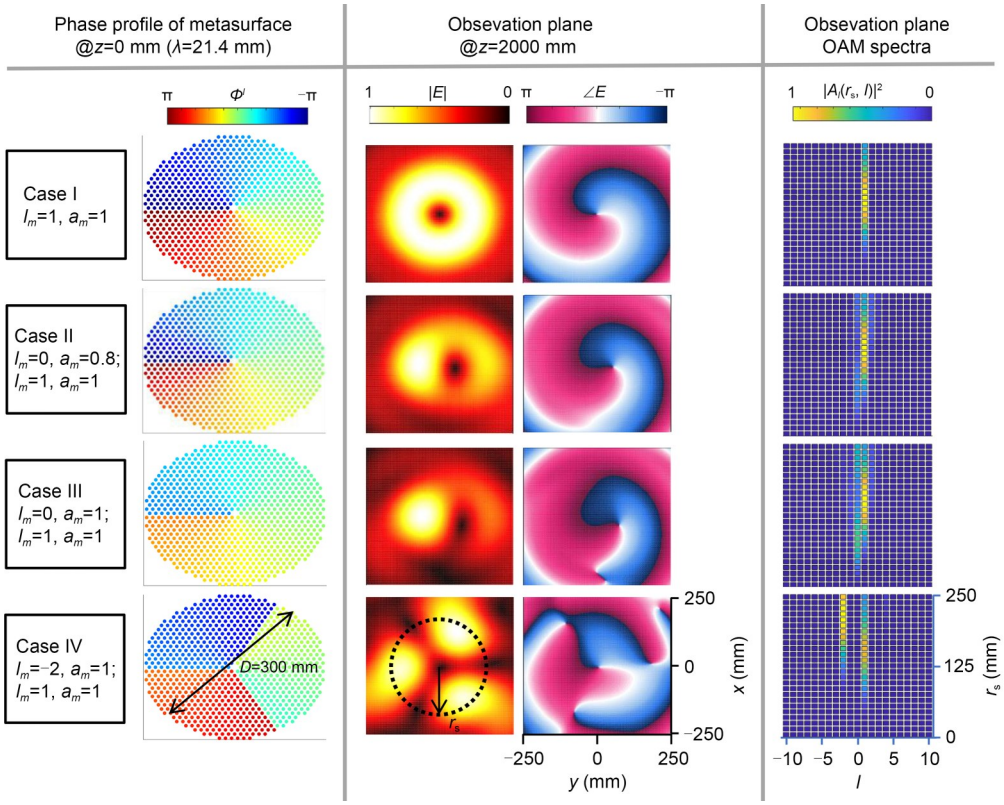

Fig. 6 Numerical results of multi-mode vortex beams generated by Eq. (4). Three columns of pictures depict different phase profiles of metasurfaces, the corresponding amplitude and phase profiles of the generated E-field at the observation plane, and the orbital angular momentum (OAM) spectra of the generated E-field, from left to right

term of mode l=0 increases, the mode energy of mode l=0 increases accordingly. Case IV shows another two-mode case, and we can conclude that the number of chipped parts in the amplitude pattern is equal to $|l_1-l_2|$ for two-mode OAM beams. In addition, we can implement Fourier transform for the generated E-field along φ at different sampling radii (r_s) to further quantify the purity and distribution of the OAM modes. The corresponding equation for OAM spectral analysis is as follows:

$$A_l(r_s,l)=\frac{1}{2\pi}\int_0^{2\pi}E(r_s,\varphi)\mathrm{e}^{-\mathrm{j}l\varphi}r_s\mathrm{d}\varphi. \tag{6}$$

As seen in Fig. 6, the OAM spectra not only verify the expected mode generation with a controllable energy weight (by a_m), but also depict the OAM energy distribution at different sampling radii (r_s). These numerical results predict our generated OAM beams, and are significant for the design of metasurfaces.

2.4 Design of circularly-polarized multiplexing multi-mode metasurface

Here, we aim to implement a CP multiplexing multi-mode metasurface using the aforementioned elements and the odd–even-phase manner. Due to the spherical wave incidence of the feed antenna, an additional compensated phase is necessary for this metasurface. The compensated phase for the i^{th} element is depicted as follows:

$$\Phi^{\mathrm{c}}=k_0\left|\boldsymbol{r}_i'-\boldsymbol{r}_{\mathrm{f}}\right|, \tag{7}$$

where $\boldsymbol{r}_{\mathrm{f}}$ is the position vector of the feed antenna. The final phase profiles (Φ_{L} and Φ_{R}) for the dual-CP waves can be obtained by phase superposition as

$$\Phi_{\mathrm{L}}=\Phi_{\mathrm{L}}^{l}+\Phi_{\mathrm{L}}^{\mathrm{c}}, \tag{8a}$$
$$\Phi_{\mathrm{R}}=\Phi_{\mathrm{R}}^{l}+\Phi_{\mathrm{R}}^{\mathrm{c}}. \tag{8b}$$

The superscripts l and c represent the mode and compensated phases, respectively

Owing to the spin-decoupled design, the metasurface can be fabricated with independent OAM beams and compensated phases for LHCP and RHCP. As seen in Fig. 1a, two offset-feed antennas (LHCP and RHCP) are employed to activate the metasurface and avoid feed blockage, generating expected vortex beams for LHCP and RHCP separately. Fig. 7 shows the specific configuration of the metasurface, which can be designed by the following process: First, the phase profiles of LHCP and RHCP (Φ_{L} and Φ_{R}) can be figured out by Eqs. (5), (7), (8a), and (8b). Second, the even- and odd-phase profiles of the metasurface (Φ_{even} and Φ_{odd}) can be calculated as follow:

$$\Phi_{\mathrm{even}}=(\Phi_{\mathrm{L}}+\Phi_{\mathrm{R}})/2, \tag{9a}$$
$$\Phi_{\mathrm{odd}}=(\Phi_{\mathrm{L}}-\Phi_{\mathrm{R}})/2. \tag{9b}$$

Finally, the metasurface can be implemented by arranging these coding elements according to the even-phase profile Φ_{even} and then rotating these coding elements according to the odd-phase profile Φ_{odd}.

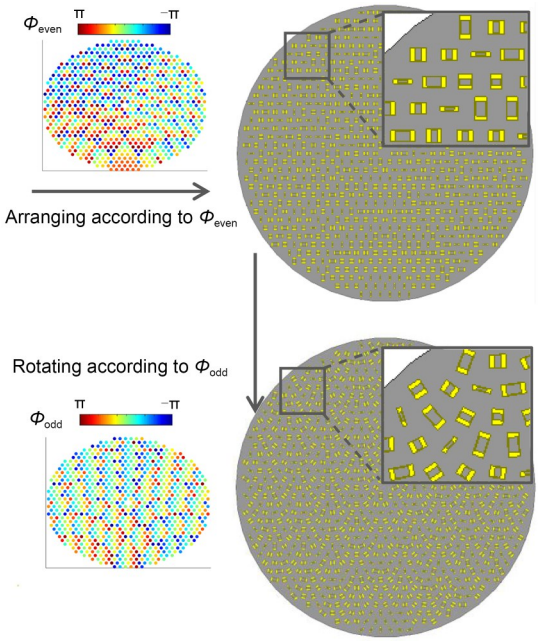

Fig. 7 Design route and specific configuration of metasurface. The parameters are l_{L}=0, a_{L}=1 and l_{L}=1, a_{L}=1, r_{fL}= [100, −150, 200] for LHCP and l_{R}=−2, a_{R}=1 and l_{R}=1, a_{R}=1, r_{fR}= [−100, −150, 200] for RHCP

2.5 Simulated results for multi-mode metasurface

To verify our proposed metasurface, we model the metasurface in commercial software HFSS and obtain the reflected field under LHCP and RHCP excitation separately (the schematic can be seen in Fig. 1a). The

amplitude profiles, phase profiles, and the corresponding spectral analysis of E-fields at the observation plane (z=2000 mm) are depicted in Fig. 8. We leave out the phase patterns and OAM spectra of the cross-polarized fields since the amplitude of the cross-polarized fields is low in this case. Under the excitation of the LHCP spiral antenna at 14 GHz, the LHCP beam dominates the energy of the reflected field and carries with expected modes with expected modes l_L={0, 1} (Fig. 8a). Fig. 8b shows the source switched to RHCP, where the main reflected field is switched to RHCP wave, and the carrying OAM modes are replaced with l_R={−2, 1} as desired. The energy of the cross-polarized field is significantly low in Figs. 8a and 8b, which contributes to the robustness and high PCR of the proposed elements. In addition, both the simulated co-polarized E-fields and the OAM spectra in Fig. 8 are highly consistent with the theoretical results in Fig. 6, which verifies the design route of dual-CP metasurface and independent generation of multi-mode vortex beams. Although the multi-mode vortex beams can be generated independently in LHCP and RHCP, the mode combinations in each CP beam are dependent or static. Independent and dynamic control over different OAM modes is still necessary for multi-mode multiplexing.

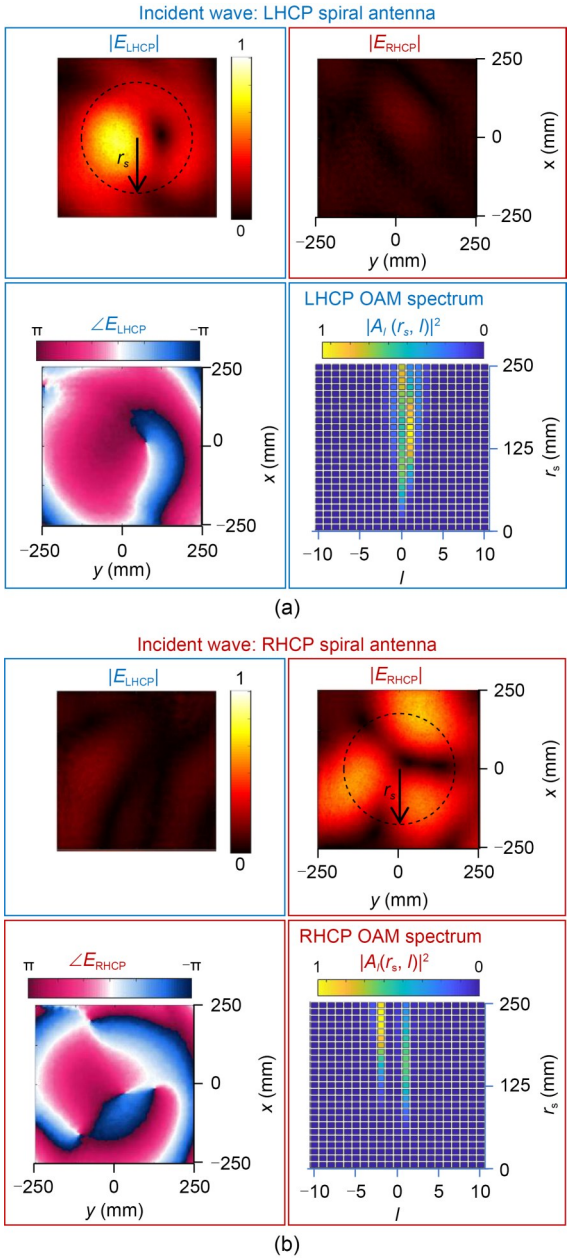

Fig. 8 Observation E-field at z=2000 mm (in HFSS) and the corresponding spectral analysis generated by spin-decoupled metasurface under excitation of different polarizations at 14 GHz: (a) left-handed circularly polarized (LHCP); (b) right-handed circularly polarized (RHCP)

2.6 Independent OAM control by multi-feed metasurfaces

Multi-feed reflectarrays have been applied to shape multiple beams or build multi-function devices (Arrebola et al., 2008). Inspired by multi-feed design, we draw a schematic of an OAM communication system in Fig. 9, where each feed antenna is assigned to manipulate different OAM modes individually. In this case, the multi-feed metasurface is configured as a multi-mode multiplexer to create a multi-cast of OAM modes. The phase profiles Φ_L and Φ_R for the dual-CP beams can be written as

$$\Phi_L(\boldsymbol{r}_i') = \angle\left(\sum_n a_{Ln} e^{jl_{Ln}\varphi_i' + jk_0|\boldsymbol{r}_i' - \boldsymbol{r}_{fLn}|}\right), \quad (10a)$$

$$\Phi_R(\boldsymbol{r}_i') = \angle\left(\sum_n a_{Rn} e^{jl_{Rn}\varphi_i' + jk_0|\boldsymbol{r}_i' - \boldsymbol{r}_{fRn}|}\right), \quad (10b)$$

where n is the number of independently controllable modes for LHCP and RHCP. l_{Ln}, l_{Rn} and a_{Ln}, a_{Rn} are the OAM modes and the corresponding amplitudes, respectively. $\boldsymbol{r}_{fLn}$ and $\boldsymbol{r}_{fRn}$ are the position vectors of the n^{th} feed antenna for LHCP and RHCP, respectively. The incident waves from different position vectors are used to generate different OAM modes, and thus $2n$ independently controllable channels can be obtained. Note that the amplitude terms (a_{Ln} and a_{Rn}) are involved for each OAM mode, providing a new degree of freedom

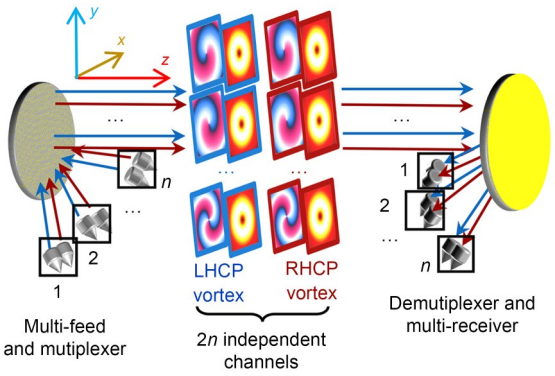

Fig. 9 Schematic for generating and receiving a multi-mode vortex beam with independent mode control based on multi-feed design

for OAM-channel control. For a proof of concept, we design a four-channel (n=2) communication system with parameters $l_{L1}=l_{R1}=-1$, $l_{L2}=l_{R2}=1$, $\boldsymbol{r}_{fL1}=[-150, -150, 200]$, $\boldsymbol{r}_{fR1}=[-100, -150, 200]$, $\boldsymbol{r}_{fL2}=[100, -150, 200]$, $\boldsymbol{r}_{fR2}=[150, -150, 200]$, and initial amplitude terms $a_{Ln}=a_{Rn}=1$. Then, the proposed multi-feed metasurface can be configured according to Eqs. (10a) and (10b), and the proposed design route is shown in Fig. 7.

The metasurface is fed by four offset-feed spiral antennas at the corresponding position vectors $\boldsymbol{r}_{fLn}$ and $\boldsymbol{r}_{fRn}$. All antennas are aligned to the center of the metasurface. Next, we can dynamically switch different OAM modes and polarization of generated beams by exciting different antennas. Fig. 9 shows the results of the generated OAM modes in simulation software, where the E-fields are sampled at the observation plane (z=2000 mm) with a size of 250 mm×250 mm, and the corresponding spectral analysis is characterized according to Eq. (6). By exciting LHCP antennas from different position vectors $\boldsymbol{r}_{fL1}$ or $\boldsymbol{r}_{fL2}$, the $l_{L1}=-1$ or $l_{L2}=1$ OAM mode is generated in LHCP reflected field (Fig. 10a). Similarly, switching the RHCP antenna between different position vectors $\boldsymbol{r}_{fR1}$ and $\boldsymbol{r}_{fR2}$ can achieve the independent generation of OAM mode $l_{R1}=-1$ or $l_{R2}=1$. The precise 2π phase shift in phase patterns and the high purity of OAM spectra verify the performance of this generator, with which we can independently generate high-purity and low cross-polarization OAM beams in the z-direction reflected field. Note that all the above phenomena are integrated on a single metasurface. Additionally, all these four OAM beams are orthogonal to each other and can be controlled independently. It means that

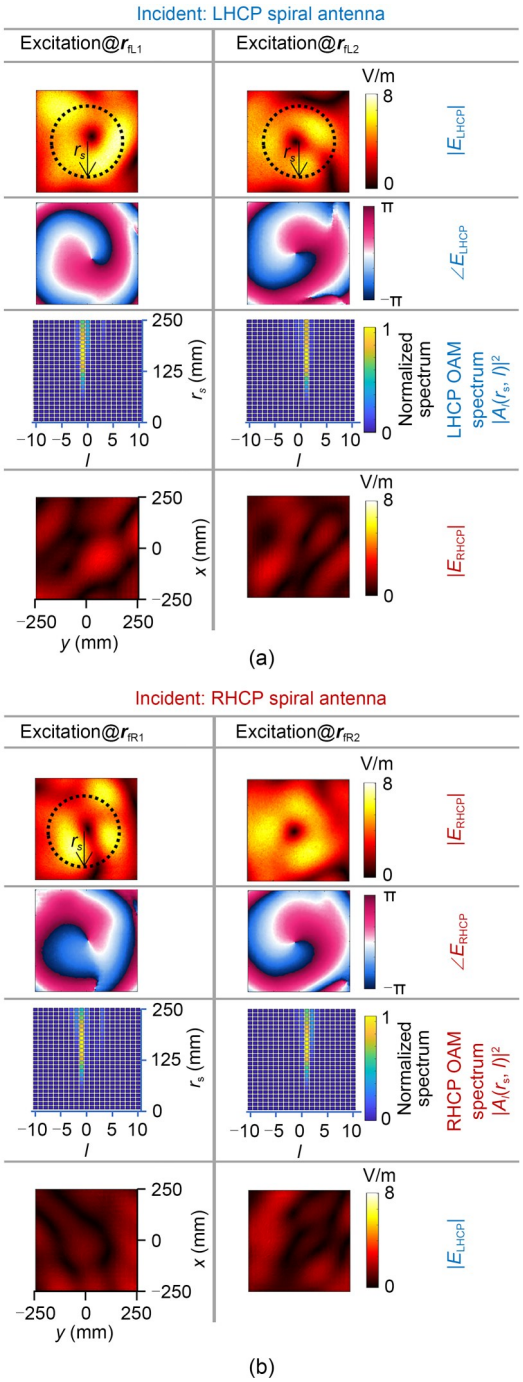

Fig. 10 Observation E-fields at z=2000 mm (in HFSS) and the corresponding spectral analysis generated by multi-feed metasurface under the offset-feed excitation at different position vectors: (a) LHCP excitation from position vector $\boldsymbol{r}_{fL1}$ and $\boldsymbol{r}_{fL2}$ separately; (b) RHCP excitation from position vector $\boldsymbol{r}_{fR1}$ and $\boldsymbol{r}_{fR2}$ separately

an arbitrary combination of these beams can be generated, transmitted, and demultiplexed with low cross-talk by a single metasurface.

3 Results

To verify the proposed metasurface experimentally, we fabricate the whole OAM generator according to the aforementioned parameters in Section 2.5. Due to the reciprocity of electromagnetic waves, the generated multi-mode vortex beams can be demultiplexed and received by the same device placed reversely at the observation plane (z=2000 mm). Fig. 11 shows the whole communication system including the front and back views of the metasurface. The ports of the transmitters and receivers are named T1–T4 and R1–R4, respectively. We transmit a continuous-wave signal over one OAM channel (T1 port), while all the other three T ports are turned off. Four S-parameters ($S_{Ri\mathrm{T}1}$) can be recorded by vector network analyzer. As seen in Fig. 12, S_{R1T1} is 9 dB higher than those of the other crosstalk channels (S_{R2T1}, S_{R3T1}, and S_{R4T1}) at operating

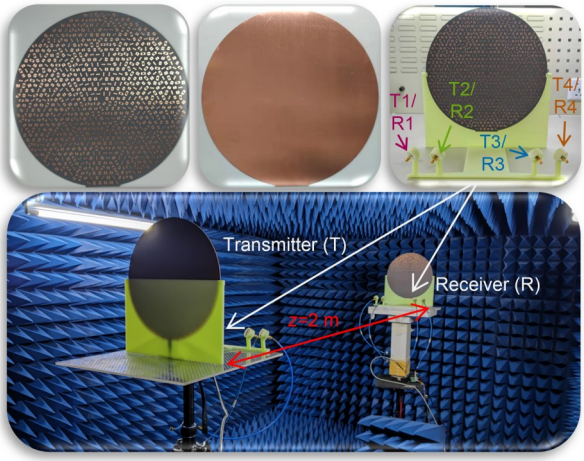

Fig. 11 Photograph of the front and back views of the fabricated metasurface, the specific multi-feed OAM generator, and the whole communication system

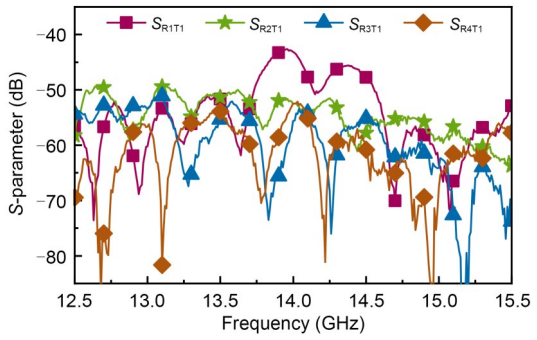

Fig. 12 Experimental S-parameters ($S_{Ri\mathrm{T}1}$) under the excitation at T1 port, while all the other three ports are turned off

frequency 14 GHz, implying that the T1-generated vortex beam can be demultiplexed and received by the R1 spiral antenna. This result also suggests that the T1 port can generate $l=-1$ LHCP vortex beam with low crosstalk. Four groups of S-parameters can be obtained by repeating the above procedure for all transmitter ports. Then, we can calculate the power transfer from recorded S-parameters for all channels as follow:

$$P_{Ri\mathrm{T}j} = 10^{S_{Ri\mathrm{T}j}/10}. \tag{11}$$

The value of $P_{Ri\mathrm{T}j}$ represents the measured power at port Ri under incident 0 dBm power from port Tj. Fig. 13a shows the corresponding powers. All the powers transmitting between different channels ($P_{Ri\mathrm{T}j}$, $i\neq j$) are significantly smaller than that in identical channels ($P_{Ri\mathrm{T}j}$, $i=j$). It not only demonstrates the natural OAM-state isolation in multiplexing/demultiplexing, but also verifies the independent control of spin and OAM states by the proposed multi-feed metasurface. A high axial ratio of the feed antennas and appropriate position vectors could further reduce the inter-mode crosstalk. Another problem that can be solved is the

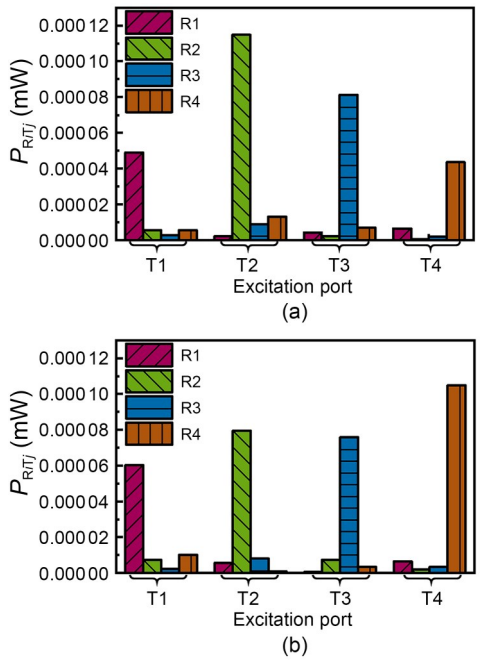

Fig. 13 Received power under the excitation of different ports at 14 GHz: (a) results of the original metasurface with amplitude terms a_{L1}=1, a_{R1}=1 and a_{L2}=1, a_{R2}=1; (b) results of the received metasurface with amplitude terms a'_{L1}=1.05, a'_{R1}=0.91 and a'_{L2}=0.95, a'_{R2}=1.09

unequal received powers for the four main channels due to the impacts including the gain difference between fed antennas, distance difference of position vectors, and misalignment between two metasurfaces. However, as seen in Fig. 6, we can adjust the amplitude terms a_n of different OAM modes to balance those channel powers. Here, the power-related adjustments of amplitude terms are provided as follows:

$$a'_{\mathrm{L1}} = a_{\mathrm{L1}} - C\frac{P_{\mathrm{R1T1}} - P_{\mathrm{R3T3}}}{P_{\mathrm{R1T1}} + P_{\mathrm{R3T3}}}, \tag{12a}$$

$$a'_{\mathrm{L2}} = a_{\mathrm{L2}} - C\frac{P_{\mathrm{R3T3}} - P_{\mathrm{R1T1}}}{P_{\mathrm{R3T3}} + P_{\mathrm{R1T1}}}, \tag{12b}$$

$$a'_{\mathrm{R1}} = a_{\mathrm{R1}} - C\frac{P_{\mathrm{R2T2}} - P_{\mathrm{R4T4}}}{P_{\mathrm{R2T2}} + P_{\mathrm{R4T4}}}, \tag{12c}$$

$$a'_{\mathrm{R2}} = a_{\mathrm{R2}} - C\frac{P_{\mathrm{R4T4}} - P_{\mathrm{R2T2}}}{P_{\mathrm{R4T4}} + P_{\mathrm{R2T2}}}, \tag{12d}$$

where C is a constant (adjustment factor) equaling 0.2 in this case. By submitting the recorded results in Fig. 13a, the adjusted amplitude terms (a'_{L1}=1.05, a'_{R1}=0.91 and a'_{L2}=0.95, a'_{R2}=1.09) can be obtained according to Eq. (12). Then we fabricate a newly adjusted metasurface to replace the original one at the receiver. Fig. 13b shows the received power in the adjusted case, where the adjusted amplitude terms balance the powers in four main channels. Although exactly equal powers cannot be obtained by one replacement of static metasurface as we did, one can iterate this adjusted process to further balance those channel powers by using a reconfigurable intelligent surface or a programmable metasurface.

4 Discussions

In this section, we further discuss the bandwidth and independent channels of our multi-feed communication system.

4.1 Bandwidth analysis for multi-feed OAM communication system

Some broadband OAM metasurfaces have been proposed under the normal incidence of a single-feed antenna. The frequency-independent phase gradient can shape broadband OAM beams. However, in the multi-feed offset case, the compensation phases in Eqs. (7) and (10) are frequency-dependent (k_0-related); the scattered wave in the offset case will deviate from the z-axis as frequency changes as seen in Fig. 14. This deviation (misalignment) is catastrophic for OAM demultiplexing. Therefore, how to integrate the frequency-independent OAM phase and the frequency-dependent compensation phase is the key point for the broadband design.

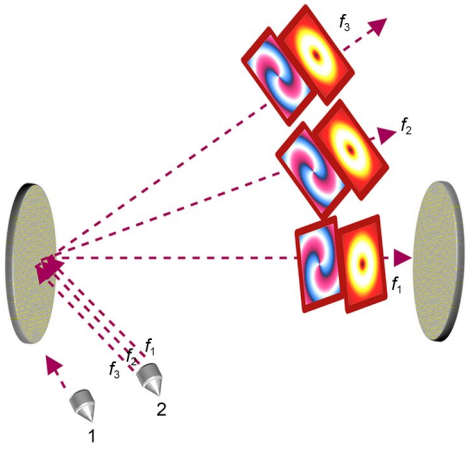

Fig. 14 Broadband performance of the off-feeding metasurfaces

4.2 Number of OAM modes independently generated

The multi-feed technology will inevitably involve an additional sidelobe in the generated OAM beams, leading to energy decay and crosstalk modes for each independently generated mode. Fig. 15 shows the l=−1 OAM beams generated by three multi-feed metasurfaces with different numbers of multiplex modes. The number of independently generated modes are n=1, n=2, and n=4. The parameters of position vectors are $\boldsymbol{r}_{\mathrm{fR1}}$=[−100, −150, 200], $\boldsymbol{r}_{\mathrm{fR2}}$=[150, −150, 200], $\boldsymbol{r}_{\mathrm{fR3}}$=[100, 150, 200], and $\boldsymbol{r}_{\mathrm{fR4}}$=[150, 150, 200]. Although, three metasurfaces can independently generate the expected l=−1 beam, the amplitude pattern and the purity of mode decrease as the number of multiplex modes (n) increases. It suggests that we cannot arbitrarily extend multiplex modes (n) under the metasurface with a fixed size. On the other hand, the configuration of position vectors is related to crosstalk modes. For example, a short distance between antennas 1 and 2 in Fig. 14 (a bad configuration of the position vectors) will make two modes indistinguishable or dependent; that is to say, no additional (distinguishable) OAM

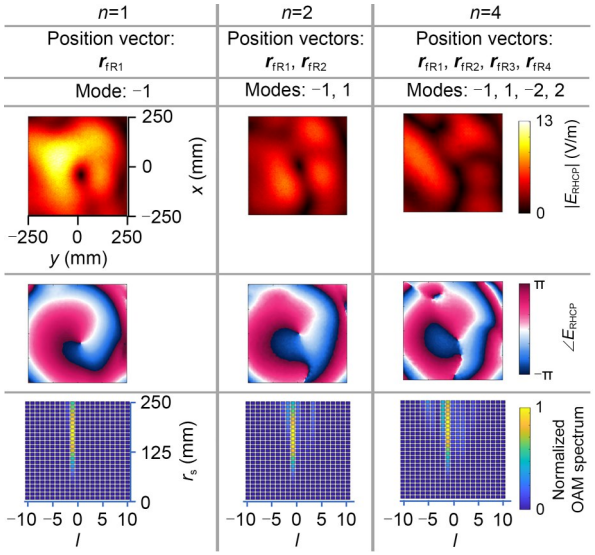

Fig. 15 Observation of the generated l=−1 OAM beams at z=2000 mm (in HFSS) and the corresponding spectral analysis generated by three multi-feed metasurfaces with different number of multiplex modes n=1, n=2, and n=4 under the excitation at position vector r_{fR1}

mode can be generated independently. Therefore, a more suitable configuration of the n position vectors (r_{f1}, r_{f2}, ⋯, r_{fn}) can reduce crosstalk in the multiplex system.

5 Conclusions

We have successfully generated vortex beams with dynamically switchable modes and polarization combinations using a single-layer multi-feed metasurface. We have proposed eight single-layer elements to control two CP phases independently. The robustness and thickness of elements have also been investigated. Additionally, the multi-feed technique has been involved to dynamically manipulate the multi-mode vortex beams and overcomes the limitation of the static OAM combination in conventional metasurfaces. Some near-field theoretical predictions and radius-related OAM spectrum analysis have been provided. Theoretical equations offer practical guidance in designing the OAM generator and receiver. Eventually, we established a four-OAM-mode communication system. The maximum crosstalk among all channels is −9 dB, verifying the high-purity OAM generation and independent CP and OAM control by the proposed OAM generator. In real-world applications, crosstalk can be further lowered by channel estimation and precoding schemes (zero-forcing, etc). Moreover, the proposed metasurface integrates the amplitude term to balance the energy distribution in different OAM modes. Since the beam patterns vary for different modes, this energy control over those modes is significant for multi-channel communication. Although the proposed system is a narrowband design working at 14 GHz, one can further improve the bandwidth by introducing a broadband design for both the compensated phase and the spin-decoupled elements. The proposed metasurface integrates dynamic multi-mode and multi-polarization manipulation, improving the compactness of devices, and can be naturally extended to other multi-function systems.

Contributors

Lingjun YANG and Sheng SUN designed the research. Lingjun YANG processed the data and drafted the paper. Sheng SUN, Wei E.I. SHA, Long LI, and Jun HU helped organize the paper. Lingjun YANG, Sheng SUN, Wei E.I. SHA, Long LI, and Jun HU revised and finalized the paper.

Compliance with ethics guidelines

Lingjun YANG, Sheng SUN, Wei E.I. SHA, Long LI, and Jun HU declare that they have no conflict of interest.

Data availability

The data that support the findings of this study are available from the corresponding author upon reasonable request.

References

Akram MR, Ding GW, Chen K, et al., 2020. Ultrathin single layer metasurfaces with ultra-wideband operation for both transmission and reflection. *Adv Mater*, 32(12):1907308. https://doi.org/10.1002/adma.201907308

Akram Z, Li XP, Qi ZH, et al., 2019. Broadband high-order OAM reflective metasurface with high mode purity using subwavelength element and circular aperture. *IEEE Access*, 7:71963-71971. https://doi.org/10.1109/ACCESS.2019.2919779

Allen L, Beijersbergen MW, Spreeuw RJC, et al., 1992. Orbital angular momentum of light and the transformation of Laguerre-Gaussian laser modes. *Phys Rev A*, 45(11): 8185-8189. https://doi.org/10.1103/PhysRevA.45.8185

Arrebola M, Encinar JA, Barba M, 2008. Multifed printed reflectarray with three simultaneous shaped beams for LMDS central station antenna. *IEEE Trans Antenn Propag*, 56(6): 1518-1527. https://doi.org/10.1109/TAP.2008.923360

Bai XD, Kong FW, Sun YT, et al., 2020. High-efficiency transmissive programmable metasurface for multimode OAM

generation. *Adv Opt Mater*, 8(17):2000570. https://doi.org/10.1002/adom.202000570

Bao YJ, Ni JC, Qiu CW, 2020. A minimalist single-layer metasurface for arbitrary and full control of vector vortex beams. *Adv Mater*, 32(6):1905659. https://doi.org/10.1002/adma.201905659

Barbuto M, Bilotti F, Toscano A, 2017. Patch antenna generating structured fields with a Möbius polarization state. *IEEE Antenn Wirel Propag Lett*, 16:1345-1348. https://doi.org/10.1109/LAWP.2016.2634081

Barbuto M, Alù A, Bilotti F, et al., 2021. Dual-circularly polarized topological patch antenna with pattern diversity. *IEEE Access*, 9:48769-48776. https://doi.org/10.1109/ACCESS.2021.3068792

Berry MV, 1984. Quantal phase factors accompanying adiabatic changes. *Proc Royal Soc A Math Phys Sci*, 392(1802): 45-57. https://doi.org/10.1098/rspa.1984.0023

Bozinovic N, Yue Y, Ren YX, et al., 2013. Terabit-scale orbital angular momentum mode division multiplexing in fibers. *Science*, 340(6140):1545-1548. https://doi.org/10.1126/science.1237861

Chen MLN, Jiang LJ, Sha WEI, 2017. Ultrathin complementary metasurface for orbital angular momentum generation at microwave frequencies. *IEEE Trans Antenn Propag*, 65(1): 396-400. https://doi.org/10.1109/TAP.2016.2626722

Chen MLN, Jiang LJ, Sha WEI, 2019. Quasi-continuous metasurfaces for orbital angular momentum generation. *IEEE Antenn Wirel Propag Lett*, 18(3):477-481. https://doi.org/10.1109/LAWP.2019.2894772

Chen YL, Zheng SL, Li Y, et al., 2016. A flat-lensed spiral phase plate based on phase-shifting surface for generation of millimeter-wave OAM beam. *IEEE Antenn Wirel Propag Lett*, 15:1156-1158. https://doi.org/10.1109/LAWP.2015.2497243

Devlin RC, Ambrosio A, Rubin NA, et al., 2017. Arbitrary spin-to–orbital angular momentum conversion of light. *Science*, 358(6365):896-901. https://doi.org/10.1126/science.aao5392

Ding GW, Chen K, Zhang N, et al., 2022. Independent wavefront tailoring in full polarization channels by helicity-decoupled metasurface. *Ann Phys*, 534(4):2100546. https://doi.org/10.1002/andp.202100546

Edfors O, Johansson AJ, 2012. Is orbital angular momentum (OAM) based radio communication an unexploited area? *IEEE Trans Antenn Propag*, 60(2):1126-1131. https://doi.org/10.1109/TAP.2011.2173142

Feng Q, Kong XD, Shan MM, et al., 2022. Multi-orbital-angular-momentum-mode vortex wave multiplexing and demultiplexing with shared-aperture reflective metasurfaces. *Phys Rev Appl*, 17(3):034017. https://doi.org/10.1103/PhysRevApplied.17.034017

Guo WL, Wang GM, Ji WY, et al., 2020a. Broadband spin-decoupled metasurface for dual-circularly polarized reflector antenna design. *IEEE Trans Antenn Propag*, 68(5): 3534-3543. https://doi.org/10.1109/TAP.2020.2963945

Guo WL, Wang GM, Luo XY, et al., 2020b. Ultrawideband spin-decoupled coding metasurface for independent dual-channel wavefront tailoring. *Ann Phys*, 532(3):1900472. https://doi.org/10.1002/andp.201900472

Han Y, Grier DG, 2003. Erratum: vortex rings in a constant electric field. *Nature*, 424(6948):510. https://doi.org/10.1038/424510b

Jiang X, Liang B, Cheng JC, et al., 2018. Twisted acoustics: metasurface-enabled multiplexing and demultiplexing. *Adv Mater*, 30(18):1800257. https://doi.org/10.1002/adma.201800257

Jiang ZH, Kang L, Yue TW, et al., 2020. A single noninterleaved metasurface for high-capacity and flexible mode multiplexing of higher-order Poincaré sphere beams. *Adv Mater*, 32(6):1903983. https://doi.org/10.1002/adma.201903983

Kang L, Li H, Zhou JZ, et al., 2019. A mode-reconfigurable orbital angular momentum antenna with simplified feeding scheme. *IEEE Trans Antenn Propag*, 67(7):4866-4871. https://doi.org/10.1109/TAP.2019.2916595

Li LL, Cui TJ, Ji W, et al., 2017. Electromagnetic reprogrammable coding-metasurface holograms. *Nat Commun*, 8(1): 197. https://doi.org/10.1038/s41467-017-00164-9

Li SQ, Li XY, Zhang L, et al., 2020. Efficient optical angular momentum manipulation for compact multiplexing and demultiplexing using a dielectric metasurface. *Adv Opt Mater*, 8(8):1901666. https://doi.org/10.1002/adom.201901666

Lin MT, Gao Y, Liu PG, et al., 2017. Theoretical analyses and design of circular array to generate orbital angular momentum. *IEEE Trans Antenn Propag*, 65(7):3510-3519. https://doi.org/10.1109/TAP.2017.2700160

Liu HQ, Teng CX, Yang HY, et al., 2018. Proposed phase plate for superimposed orbital angular momentum state generation. *Opt Expr*, 26:14792-14799. https://doi.org/10.1364/OE.26.014792

Liu K, Liu HY, Qin YL, et al., 2016. Generation of OAM beams using phased array in the microwave band. *IEEE Trans Antenn Propag*, 64(9):3850-3857. https://doi.org/10.1109/TAP.2016.2589960

Liu K, Cheng YQ, Gao Y, et al., 2017. Super-resolution radar imaging based on experimental OAM beams. *Appl Phys Lett*, 110(16):164102. https://doi.org/10.1063/1.4981253

Luo WJ, Sun SL, Xu HX, et al., 2017. Transmissive ultrathin pancharatnam-berry metasurfaces with nearly 100% efficiency. *Phys Rev Appl*, 7(4):044033. https://doi.org/10.1103/PhysRevApplied.7.044033

Ma LN, Chen C, Zhou LY, et al., 2019. Single-layer transmissive metasurface for generating OAM vortex wave with homogeneous radiation based on the principle of Fabry-Perot cavity. *Appl Phys Lett*, 114(8):081603. https://doi.org/10.1063/1.5081514

Menzel C, Rockstuhl C, Lederer F, 2010. Advanced Jones calculus for the classification of periodic metamaterials. *Phys Rev A*, 82(5):053811. https://doi.org/10.1103/PhysRevA.82.053811

Mohammadi SM, Daldorff LKS, Bergman JES, et al., 2010. Orbital angular momentum in radio—a system study. *IEEE Trans Antenn Propag*, 58(2):565-572. https://doi.org/10.1109/TAP.2009.2037701

Mueller JPB, Rubin NA, Devlin RC, et al., 2017. Metasurface

polarization optics: independent phase control of arbitrary orthogonal states of polarization. *Phys Rev Lett*, 118(11): 113901. https://doi.org/10.1103/PhysRevLett.118.113901

Pitilakis A, Seckel M, Tasolamprou AC, et al., et al., 2022. Multifunctional metasurface architecture for amplitude, polarization and wave-front control. *Phys Rev Appl*, 17(6): 064060. https://doi.org/10.1103/PhysRevApplied.17.064060

Pogorzelski RJ, 2004. Phased arrays based on oscillators coupled on triangular and hexagonal lattices. *IEEE Trans Antenn Propag*, 52(3):790-800. https://doi.org/10.1109/TAP.2004.825489

Shuang Y, Zhao HT, Ji W, et al., 2020. Programmable high-order OAM-carrying beams for direct-modulation wireless communications. *IEEE J Emerg Sel Top Circ Syst*, 10(1):29-37. https://doi.org/10.1109/JETCAS.2020.2973391

Sievenpiper D, Zhang LJ, Broas RFJ, et al., 1999. High-impedance electromagnetic surfaces with a forbidden frequency band. *IEEE Trans Microw Theory Techn*, 47(11): 2059-2074. https://doi.org/10.1109/22.798001

Sroor H, Huang YW, Sephton B, et al., 2020. High-purity orbital angular momentum states from a visible metasurface laser. *Nat Photon*, 14(8):498-503. https://doi.org/10.1038/s41566-020-0623-z

Sun SL, He Q, Xiao SY, et al., 2012. Gradient-index meta-surfaces as a bridge linking propagating waves and surface waves. *Nat Mater*, 11(5):426-431. https://doi.org/10.1038/NMAT3292

Tamagnone M, Craeye C, Perruisseau-Carrier J, 2012. Comment on 'encoding many channels on the same frequency through radio vorticity: first experimental test'. *New J Phys*, 14: 118001. https://doi.org/10.1088/1367-2630/14/11/118001

Tang SW, Cai T, Liang JG, et al., 2019. High-efficiency transparent vortex beam generator based on ultrathin Pancharatnam–Berry metasurfaces. *Opt Expr*, 27(2):1816-1824. https://doi.org/10.1364/OE.27.001816

Thidé B, Then H, Sjöholm J, et al., 2007. Utilization of photon orbital angular momentum in the low-frequency radio domain. *Phys Rev Lett*, 99(8):087701. https://doi.org/10.1103/PhysRevLett.99.087701

Tian HW, Jiang WX, Li X, et al., 2019. Generation of high-order orbital angular momentum beams and split beams simultaneously by employing anisotropic coding metasurfaces. *J Opt*, 21(6):065103. https://doi.org/10.1088/2040-8986/ab16b9

Uribe-Patarroyo N, Alvarez-Herrero A, López Ariste A, et al., 2011. Detecting photons with orbital angular momentum in extended astronomical objects: application to solar observations. *A&A*, 526:A56. https://doi.org/10.1051/0004-6361/201014844

Vellucci S, Longhi M, Monti A, et al., 2022. Antenna pattern shaping through functionalized metasurface coatings. Proc Sixteenth Int Congress on Artificial Materials for Novel Wave Phenomena, p.466-468. https://doi.org/10.1109/Metamaterials54993.2022.9920784

Wang J, Yang JY, Fazal IM, et al., 2012. Terabit free-space data transmission employing orbital angular momentum multiplexing. *Nat Photon*, 6(7):488-496. https://doi.org/10.1038/nphoton.2012.138

Wang ZX, Wu JW, Wu LW, et al., 2021. High efficiency polarization-encoded holograms with ultrathin bilayer spin-decoupled information metasurfaces. *Adv Opt Mater*, 9(5): 2001609. https://doi.org/10.1002/adom.202001609

Xu HX, Liu HW, Ling XH, et al., 2017. Broadband vortex beam generation using multimode Pancharatnam–Berry metasurface. *IEEE Trans Antenn Propag*, 65(12):7378-7382. https://doi.org/10.1109/TAP.2017.2761548

Xu HX, Hu GW, Jiang MH, et al., 2020. Wavevector and frequency multiplexing performed by a spin-decoupled multichannel metasurface. *Adv Mater Technol*, 5(1):1900710. https://doi.org/10.1002/admt.201900710

Yan Y, Xie GD, Lavery MPJ, et al., 2014. High-capacity millimetre-wave communications with orbital angular momentum multiplexing. *Nat Commun*, 5:4876. https://doi.org/10.1038/ncomms5876

Yang LJ, Sun S, Sha WEI, 2020. Ultrawideband reflection-type metasurface for generating integer and fractional orbital angular momentum. *IEEE Trans Antenn Propag*, 68(3): 2166-2175. https://doi.org/10.1109/TAP.2019.2948711

Yang LJ, Sun S, Sha WEI, 2021. Manipulation of orbital angular momentum spectrum using shape-tailored metasurfaces. *Adv Opt Mater*, 9(2):2001711. https://doi.org/10.1002/adom.202001711

Yang LJ, Sun S, Sha WEI, et al., 2022. Arbitrary vortex beam synthesis with donut-shaped metasurface. *IEEE Trans Antenn Propag*, 70(1):573-584. https://doi.org/10.1109/TAP.2021.3098604

Yang LJ, Sun S, Sha WEI, et al., 2023. Bifunctional integration performed by a broadband high-efficiency spin-decoupled metasurface. *Adv Opt Mater*, 11(2):2201955. https://doi.org/10.1002/adom.202201955

Yu NF, Genevet P, Kats MA, et al., 2011. Light propagation with phase discontinuities: generalized laws of reflection and refraction. *Science*, 334(6054):333-337. https://doi.org/10.1126/science.1210713

Yu SX, Li L, Shi GM, et al., 2016a. Design, fabrication, and measurement of reflective metasurface for orbital angular momentum vortex wave in radio frequency domain. *Appl Phys Lett*, 108(12):121903. https://doi.org/10.1063/1.4944789

Yu SX, Li L, Shi GM, et al., 2016b. Generating multiple orbital angular momentum vortex beams using a metasurface in radio frequency domain. *Appl Phys Lett*, 108(24):241901. https://doi.org/10.1063/1.4953786

Yuan SSA, Wu J, Chen MLN, et al., 2021. Approaching the fundamental limit of orbital-angular-momentum multiplexing through a hologram metasurface. *Phys Rev Appl*, 16(6): 064042. https://doi.org/10.1103/PhysRevApplied.16.064042

Yuan YY, Sun S, Chen Y, et al., 2020. A fully phase-modulated metasurface as an energy-controllable circular polarization router. *Adv Sci*, 7(18):2001437. https://doi.org/10.1002/advs.202001437

Zhang K, Yuan YY, Zhang DW, et al., 2018. Phase-engineered metalenses to generate converging and non-diffractive vortex beam carrying orbital angular momentum in microwave region. *Opt Expr*, 26(2):1351-1360. https://doi.org/10.1364/OE.26.001351

Zhang S, Huo PC, Zhu WQ, et al., 2020. Broadband detection of multiple spin and orbital angular momenta via dielectric metasurface. *Laser Photon Rev*, 14(9):2000062. https://doi.org/10.1002/lpor.202000062

Zhang WT, Zheng SL, Hui XN, et al., 2017. Four-OAM-mode antenna with traveling-wave ring-slot structure. *IEEE Antenn Wirel Propag Lett*, 16:194-197. https://doi.org/10.1109/LAWP.2016.2569540

Zhang XG, Jiang WX, Jiang HL, et al., 2020. An optically driven digital metasurface for programming electromagnetic functions. *Nat Electron*, 3(3):165-171. https://doi.org/10.1038/s41928-020-0380-5

Zhang ZF, Zheng SL, Jin XF, et al., 2017. Generation of plane spiral OAM waves using traveling-wave circular slot antenna. *IEEE Antenn Wirel Propag Lett*, 16:8-11. https://doi.org/10.1109/LAWP.2016.2552227

Zhu L, Wang J, 2015. Simultaneous generation of multiple orbital angular momentum (OAM) modes using a single phase-only element. *Opt Expr*, 23(20):26221-26233. https://doi.org/10.1364/OE.23.026221